

# Carbon-based nanostructured composite films: elastic, mechanical and optoelectronic properties derived from computer simulations

Maria Fyta<sup>a,1,\*</sup>, Christos Mathioudakis<sup>a,2</sup>, Ioannis N. Remediakis<sup>a,3</sup>, Pantelis C. Kelires<sup>a,4</sup>

<sup>a</sup>*Physics Department, University of Crete, P.O. Box 2208, 710 03, Heraklion, Crete, Greece*

---

## Abstract

In this review, we present our recent computational work on carbon-based nanostructured composites. These materials consist of carbon crystallites embedded in an amorphous carbon matrix and are modeled here through classical and semi-empirical quantum-mechanical simulations. We investigate the energetics, mechano-elastic, and optoelectronic properties of these materials. Once the stability of the composites is discussed, we move on to the calculation of their elastic moduli and constants, their anisotropy and elastic recovery. At a next step, we focus on diamond composites, which were found to be the most stable among the composites studied, and went beyond the elastic regime to investigate their ideal fracture. Finally, for these materials, the electronic density of states, dielectric function, and optical response were calculated and linked to the disorder in the structures. Our findings unveil the high potential of these materials in nanotechnological applications, especially as ultra-hard coatings.

**Keywords:** carbon nanocomposites, amorphous carbon, nanotubes, mechanical properties, optoelectronic properties

---



---

\*Corresponding author

*Email addresses:* mfyta@ph.tum.de (Maria Fyta), chr@materials.uoc.gr (Christos Mathioudakis), remed@materials.uoc.gr (Ioannis N. Remediakis), pantelis.kelires@cut.ac.cy (Pantelis C. Kelires)

<sup>1</sup>Present address: Department of Physics, Technical University of Munich, Garching, Germany

<sup>2</sup>Present address: Department of Materials Science and Technology, University of Crete, Heraklion, Crete, Greece

<sup>3</sup>Present address: Department of Materials Science and Technology, University of Crete, Heraklion, Crete, Greece

<sup>4</sup>Present address: Department of Mechanical Engineering and Materials Science and Engineering, Cyprus University of Technology, Limassol, Cyprus

## 1. Introduction

Carbon-based nanostructured composites (*na-C*) [1, 2] are believed to intermingle properties of carbon nanostructures with those of single-phase amorphous carbon (*a-C*) [3]. These nanocomposites are hybrid forms of carbon in which nanocrystallites are embedded in the *a-C* matrix. In this sense, their properties can be tailored by controlling the type and size of the embedded structures, as well as the matrix material. Such composites, also investigated in this work, are relevant to both bulk and thin film materials.

A variety of carbon nanostructures can compose *na-C*, ranging from diamond crystallites, to entirely three-dimensional  $sp^2$  covalent conformations with no dispersion/van der Waals (vdW) bonding, i.e. open graphene structures with negative curvature (schwarzites) [4, 5, 6], to carbon nanotubes (CNT) [7] bound by vdW forces. *Na-C* films have been synthesized before by using different methods [8]. The synthesis of nanodiamond composites (*nD/a-C*) and its growth mechanisms have been explored in both hydrogenated [9, 10] and pure [11, 12] tetrahedral amorphous carbon (*ta-C*) matrices.

Here, we review our recent theoretical and simulational studies of nanostructured carbon films, which shed light on their mechanical and optoelectronic properties. This review is organized as follows: Section 2 outlines the methodology followed here. Section 3 discusses the energetics and stability of all modeled nanocomposites. The elastic and mechanical properties of diamond and nanotube composites are investigated in section 4. The ideal fracture and optoelectronic properties of diamond nanocomposites are discussed in sections 5, 6. We summarize in section 7.

## 2. Methodology

We have recently followed a theoretical approach to investigate *na-C* and unravel the fundamental principles governing the interaction of nanostructures with the *a-C* matrix (see for example [13, 14]). Two different methods were used, a Monte Carlo (MC) method within the Tersoff empirical potential approach [15], and a tight-binding molecular dynamics (TBMD) scheme which utilizes separately two hamiltonians, the Mehl & Papaconstantopoulos [16, 17] (TB-NRL), and the environment-dependent (EDTB) Wang & Ho [18] model. The former employs non-orthogonal atomic orbitals, while the latter goes beyond the traditional two-center approximation and allows the tight-binding parameters to change according to the bonding environment. Using both the MC and TBMD, one is able to combine higher statistical precision with higher accuracy and bridge the gap between classical and first-principles calculations. Both the Tersoff potential, as well as the two hamiltonians have been used to successfully model the interatomic interactions in various crystalline and amorphous carbon forms [19, 20, 21, 22, 23]

The TBMD simulations are carried out in the canonical ( $N, V, T$ ) ensemble. The volume  $V$  and the number of particles (atoms)  $N$  are constant. Dispersion/van der Waals (vdW) forces within the Tersoff potential approach, will

be included by adding a simple Lennard-Jones potential, which successfully describes properties of carbon nanocrystals [24, 25]. The parameters used for this potential are  $\epsilon = 2.964 \text{ meV}$  and  $\sigma = 3.407 \text{ \AA}$ .

For the calculation of the optoelectronic properties the EDTB scheme was used, which has proved to be quite efficient in similar cases [22]. The electronic structure can be easily extracted and is directly correlated to the imaginary part  $\varepsilon_2$  of the complex dielectric function. This in turn yields the optical gaps and absorption coefficient, which further link to the disorder in the structures through the Urbach energy. Additional details can be found elsewhere [26].

### 2.1. Structure generation

We have generated the nanocomposites studied here by melting and subsequent quenching at constant volume various carbon crystalline cells, while keeping a certain number of atoms in the central portion of the cells frozen in their ideal crystal positions. Consequently, the cells are thoroughly relaxed with respect to atomic positions and density. For the nanotube composites, a core is removed from a diamond crystal leaving a void with a shape similar to that of the nanotube, in which the nanotube is then placed. Details can be found in Ref. [13, 14].

The total number of atoms in the structures ranges from  $\sim 2500$  to  $4536$ , and the number of atoms in the nanocrystals ranges from  $\sim 300$  to  $900$ . The size of the computational cells ranges from about  $1.5$  to  $4.0 \text{ nm}$ . For the TBMD relaxed structures we use smaller cells up to  $512$  atoms. The diameter ( $d$ ) of all crystalline inclusions used are in the range  $d=0.6\text{-}2.8 \text{ nm}$ . Periodic boundary conditions (PBC) are applied to the cells. The exact details for each composite studied with the Tersoff potential are summarized in Table 1. Diamond inclusions are almost spherical, while CNTs have open ends and extend through the entire length of the cube. Due to the PBC, this corresponds to a dense array of CNTs packed in parallel, which is an idealized model of a CNT nanocomposite. However, this model captures all essential features of the CNT-matrix interaction resembles CNT bundles with *a*-C material in between the tubes.

Representative structures of a specific group of conformations are chosen and embedded in amorphous matrices: the  $sp^3$  conformations (a) Diamond (D), and the (b) high-pressure phase BC8 structure for carbon, the negatively-curved  $sp^2$  conformations with a  $D$  periodic minimal surface, (c) polybenzene ( $6.8^2 D$ ) [4], (d) PCCM (porous conducting carbon modification), an  $sp^2$ -bonded structure with eightfold rings [27], (e)  $C_{168}$ , a low-density, negative-curvature schwarzite structure [5], (f) the positively curved  $sp^2$  carbon nanotubes (CNT) [7] with single (SWNT) and multiple (MWNT) graphitic walls. Structures (c)-(e) do not involve vdW bonding. In Fig.1, representative nanocomposites of the ones studied here are shown: a diamond of  $1.70 \text{ nm}$  diameter, a  $C_{168}$ , and a  $(7,10)$  SWNT of  $1.17 \text{ nm}$  diameter, embedded in a highly tetrahedral ( $z_{am} \simeq 3.8$ ,  $\rho \simeq 3.3 \text{ g cm}^{-3}$ ) and low density ( $z_{am} \simeq 2.8$ ,  $\rho \simeq 1.5 \text{ g cm}^{-3}$ , and  $z_{am} \simeq 3.2$ ,  $\rho \simeq 2.2 \text{ g cm}^{-3}$ , respectively) matrices. The mean coordination of the amorphous matrix and the total density of the composites are denoted  $z_{am}$  and  $\rho$ , respectively. Fig.1(b) shows clearly, that no covalent bonding between CNT

atoms and the matrix exists, as the vdW forces drive a reconstruction of the surrounding medium, producing a graphitic wall at a distance of 3.4 Å from the CNT.

### 3. Formation Energies

We begin with the investigation of the stability of the nanocomposites studied here. The interaction of the embedded configuration with the host is taken care of by defining the formation energy of a nanocrystal, given by

$$E_{form} = E_{total} - N_a E_a - N_c E_c \quad (1)$$

In this equation,  $E_{total}$ ,  $E_c$  are the total cohesive energies per atom of the composite system and the crystalline phase, respectively.  $N_c$ ,  $N_a$  are the number of atoms in the nanocrystal, and the amorphous matrix, respectively, and  $E_a$  is the cohesive energy per atom of the pure amorphous phase (without the nanocrystal) with coordination  $z_{am}$  [13]. A negative value of  $E_{form}$  denotes stability of the nanostructure, a positive value indicates metastability.

The formation energies, hence stabilities, of all nanocomposites in this study are depicted in Fig.2. Of the nanostructures considered, only diamond and the C<sub>168</sub> schwarzite are stable ( $E_{form} < 0$ ), the former at high  $z_{am}$  ( $\rho_{am} \geq 3 \text{ gcm}^{-3}$ ), the latter at low  $z_{am}$  ( $\rho_{am} \leq 1.2 \text{ gcm}^{-3}$ ). Both crystallites are stable in a matrix with structural characteristics similar to their own, which relates to a small density gradient between the matrix and the inclusion: diamonds(schwarzites) are dense  $sp^3$ (low density  $sp^2$ ) networks, thus are embedded in a dense(dilute) matrix. A small density gradient does not give rise to discontinuities and thereby energetically favors the embedding of the crystalline inclusion. Overall, diamonds are more stable than schwarzites. Their enhanced stability in highly tetrahedral networks indicates that once nucleation centers are formed large diamond regions can be further grown, as shown in experiments [9, 10]. Through annealing of the diamond composites, an unstable structure extensively shrinks, and only a small core remains intact, while the stable structure retains its shape and should expand. Metastable diamonds are on the average larger, but more deformed, than stable diamonds in *ta*-C. For a better nanostructured material it is preferable to nucleate diamond cores in a *ta*-C matrix.

All other nanostructures studied in this work are metastable ( $E_{form} > 0$ ) through the whole coordination range. Their curves exhibit a well defined local minimum at which  $E_{form}$  is quite small, suggesting that they can be maintained in the amorphous matrix under moderate conditions and their synthesis is possible. The fact that  $E_{form}$  for 6.8<sup>2</sup>*D* and PCCM composites are only slightly lower than that for a diamond inclusion suggests the possibility of a phase transformation of  $sp^2$ -bonded structures to diamond under the proper conditions of pressure and temperature. This would subsequently aid the experiments towards synthesis of such theoretical carbon crystals. More details are discussed in [13]. CNT composites are also metastable with minima in their  $E_{form}$  at intermediate coordinations  $z_{am}$ .

## 4. Elastic and mechanical properties

The elastic and mechanical properties of carbon composites are important for potential applications as ultra-hard protective or biomedical coatings. We focus on diamond nanocomposites ( $nD/a-C$ ), which are the most stable among the ones we dealt with in this work, and the nanotube nanocomposites ( $CNT/a-C$ ), as a representative  $sp^2$  structure with positive curvature which is of wide technological interest.

### 4.1. Bulk and Young's moduli

We begin with the calculations of the bulk modulus ( $B$ ), which was calculated by fitting the energy vs volume curve after a hydrostatic deformation to the Birch-Murnacham equation [28]. Figs. 3(a), 4(a) show the calculated moduli plotted as a function of the nanocomposite density for various diamond and nanotube diameters, respectively. The bulk modulus is significantly enhanced with increasing density and inclusion size. Replacement of some amorphous material by crystalline increases noticeably the bulk modulus, with respect to  $B$  of  $a-C$ , in both diamond [23] and nanotube composites (Fig.4(a)).  $B$  for some samples is even higher than that of the *amorphous diamond* network (WWW) [29] and close to that of diamond [23]. A similar enhancement of the hardness with the grain size was found in ultra-nanocrystalline diamond [30] and copper films [31]. A comparison of  $B$  for SWNT and MWNT inclusions of the same diameters embedded in  $a-C$  of similar densities reveals, that the number of walls that consist a MWNT is crucial for the whole composite's rigidity (see Fig.4(b)). By increasing the number of graphitic walls within a CNT the composite becomes more rigid.

A check whether the rule of mixtures [32] applies to diamond and CNT composites revealed that it indeed holds for the former, but not for the latter structures. Apparently, the CNT composites are significantly influenced by the presence of the matrix. In these structures, the microstructural details of the matrix have been significantly altered with respect to pure  $a-C$ . We note again, that the effect of the inclusion is to drive the surrounding matrix atoms further away from the nanotube and stabilize them at a distance of about 3.4 Å. On the other hand, no such a significant effect was evident in  $nD/a-C$ , as there is a smooth structural transition from the inclusion to the matrix. In other words, there is a direct connection of the inclusion-matrix bonding and the validity of the rule of mixtures: in the nanotube composites the bonding between the matrix and the inclusion is of a van der Waals type and the rule does not hold, while in the diamond composites the two phases are covalently bonded and this rule still holds.

The trends for the Young's moduli ( $Y$ ), which is easily extracted from the elastic constants discussed next, of both composites are the same as in the case of  $B$ . For  $nD/a-C$ ,  $Y$  is shown in Fig.3. A considerable enhancement of  $Y$  was found, especially in high density matrices, with values approaching that for diamond [23]. In the case of  $CNT/a-C$ , a marked characteristic is the high

elastic anisotropy which is monitored by the ratio

$$A = Y_{\perp}/Y_{\parallel} \quad (2)$$

where  $Y_{\parallel}$ ,  $Y_{\perp}$  are the components of  $Y$  in the direction of the tube (axial) and in the transverse directions. A composite with a SWNT with diameter of 1.65 nm and a density of 1.99 g cm<sup>-3</sup> (2.14 g cm<sup>-3</sup>) has  $Y_{\parallel} = 478(564)$  GPa and  $Y_{\perp} = 231(306)$  GPa, yielding  $A = 0.48(0.54)$ . The anisotropy increases with increasing tube diameter, as the tube contribution overwhelms the isotropic matrix part.

#### 4.2. Elastic constants

To supplement the calculation of  $B$ , the remaining elastic moduli are computed. All simulation cells of the diamond composites are cubic systems, thus only the knowledge of the  $c_{11}$ ,  $c_{12}$  and  $c_{44}$  is needed. This is not exactly the case for CNT composites, as these are modeled through tetragonal computational cells. To calculate the elastic constants, we apply the appropriate deformation to the system and compute its total energy as a function of the imposed strain. The curvature of this function at its minimum yields the desired modulus. The results are plotted in Fig.3(b) as a function of the density for diamond composites. All elastic constants increase with increasing density. This is also the case in CNT/*a*-C, for which representative values are summarized in Table 2. For an isotropic material,

$$\eta = \frac{c_{11} - c_{12}}{2c_{44}} = 1 \quad (3)$$

which holds within 4% or less, for *nD/a*-C. For a typical CNT composite,  $\eta = 0.75$ , while for all pure *a*-C networks  $\eta = 0.98$ .

We have also looked at the elastic recovery during a compression-decompression cycle from 0 to 100 GPa for diamond and nanotube composites (with inclusions of sizes 1.7 nm and 1.2 nm, respectively), as well as for amorphous structures [33]. The elastic recovery of *nD/a*-C and single-phase *a*-C is almost perfect in the highly tetrahedral regime (*ta*-C), but is not perfect as the  $sp^3$  fraction declines. An almost fully  $sp^2$ -bonded *a*-C network regains its initial volume at about 95 %. A CNT composite, having a high  $sp^2$  fraction does not fully recover and shows a hysteresis in the compression curves. Our results indicate that the compressibility from CNT/*a*-C towards *a*-C and *nD/a*-C is decreasing, as long as the  $sp^2$  fraction remains high.

### 5. Ideal strength of diamond nanocomposites

A study beyond the elastic regime gives an insight to the ideal fracture of *a*-C and *nD/a*-C. Tensile (along diamond's easy slip {111} plane) and shear (on the {111} plane in a  $\langle 112 \rangle$  direction) loads were applied and the stress versus strain curves were extracted. The NRL hamiltonian at low temperature was used in this study. This method has already been tested in the case of diamond and the findings compared well with previous *ab initio* results [34, 35].

Three *a*-C samples were considered (a typical non-hydrogenated *a*-C with  $z_{am}=3.47$ , a *ta*-C sample with  $z_{am}=3.78$  and a WWW sample) and a *nD/a*-C with an inclusion of about 1.2 nm embedded in *ta*-C with an  $sp^2$  fraction of about 30%. The stress vs. strain curves in the case of the tensile load are summarized in Fig.5, left panel. The maximum stresses are roughly 60, 40, 30, and 124 GPa for  $z_{am}=4.00$ , 3.78, 3.47, and diamond, respectively. Thus, the ideal strength of *a*-C is proportional to its  $sp^3$  ratio. The stress vs. strain curves for the low-density *a*-C ( $sp^3$  fraction  $\sim 50\%$ ) sample suggest a ductile behavior. The fracture of *a*-C, which has an ideal strength half that of *ta*-C, takes place at a higher load than *ta*-C, i.e. larger strain needs to be applied to break the *a*-C network. Similar are the results when a shear load is applied.

For the diamond composite, the easy slip plane of the embedded diamond core was not found to play a crucial role in the total strength and no weak directions were present. The crystalline phase remains unaffected by the external load, which is almost completely taken by the surrounding amorphous matrix. The response, thus, of *nD/a*-C to external load beyond the elastic regime is identical to the response of the embedding matrix. The onset of fracture takes place at the weakly bonded  $sp^3$  sites in the amorphous matrix [23]. Bonds in the crystal are at this point actually elongated. Fracture in diamond nanocomposites is inter-grain and their ideal strength is similar to the pure amorphous phase. A snapshot of a *nD/a*-C at the onset of fracture (i.e. at the maximum stress) is shown in Fig.5, right panel.

## 6. Optoelectronic properties

Finally, focus is given on the electronic and optical properties of diamond nanocomposites. We were able to probe at a local atomic level the optoelectronic response of the composite and link it to the associated disorder, which exists at the interface between the diamond inclusions and the embedding *a*-C matrix. This can be quantitatively probed by extracting the Urbach energies from the optical parameters. Disorder in the nanocrystals appears in their outer shell near the interface and is manifested as bond length and angle distortions.

As representative quantities of an analysis done elsewhere [26], the electronic density of states (EDOS) and the imaginary part ( $\epsilon_2$ ) of the dielectric function for *nD/a*-C are shown in Fig.6. The same approach for the study of the dielectric response for diamond-like amorphous carbon has been used before [36]. The results compare qualitatively well with recent experiments [37], taking into account that in the latter case the diamond-like film was hydrogenated. A first look at the EDOS in Fig.6 reveals that the main contribution to the formation of the gap, i.e. the absence of electronic states, and of any states located in the gap region comes from the amorphous matrix part, as this has a lower energy gap than diamond due to the presence of  $sp^2$  hybrids. As the  $sp^2$  ratio, which controls the gap through the separation of  $\pi$ - $\pi^*$  bonding-antibonding states increases, the gap region shrinks. A smaller contribution to the gap states originates from distorted  $sp^3$  atoms of the diamond inclusion at the interface.

Decomposition of the total  $\varepsilon_2$  into contributions from the atoms in the crystalline and amorphous regions showed, that the optical response of the nanocomposite system is progressively varied. This variation occurs as the  $\text{sp}^2$  fraction in the amorphous part is increased from having nearly diamond-like nature to having nearly graphite-like nature. It was also clear that the energy gaps, i.e. absence of electronic transitions at the edge of the spectra, are reduced as the  $\text{sp}^2$  fraction increases. Near the gap the main contribution comes from transitions between states localized in atoms of the amorphous part.

Calculation of the Urbach energy ( $E_U$ ) in  $n\text{D}/a\text{-C}$ , which is linked directly to the optical response provides information about the disorder in the structure. We have recently shown [38], that  $E_U$  is a good measure of disorder in  $a\text{-C}$ , as it reflects not only bond-length and bond-angle distortions (structural disorder), but also topological disorder related to the size distribution of chains and clusters of  $\text{sp}^2$  and  $\text{sp}^3$  atoms in the mixed phase [3]. Thus, it is a measure of the inhomogeneous disorder in the two-phase network. For example, in highly tetrahedral  $ta\text{-C}$ , the larger the  $\text{sp}^2$  cluster sizes the higher the  $E_U$  values. This is because the embedding of minority configurations into a host phase produces disorder, which is reflected in the  $\pi\text{-}\pi^*$  subgap transitions. We also showed [38] that transitions between states localized on unpaired  $\text{sp}^2$  sites (dangling bonds), or between such states and neighboring  $\pi$  or  $\sigma$  states, are negligible. This is in contrast to  $a\text{-Si:H}$ , where dangling bond defects are the main contributors to the Urbach edge.

$E_U$  for a typical composite is shown in Fig.7 and underlines a nonmonotonic behavior for both the composite and pure  $a\text{-C}$ . The variation of  $E_U$  in the case of  $n\text{D}/a\text{-C}$  comes from the atoms in the matrix, but with higher values at the maximum of the variation and at the tetrahedral region, indicating the excess disorder produced on these atoms. We have also broken  $E_U$  down into atomic components by calculating separately the absorption coefficient ( $\alpha$ ) contributed by the atoms close to the diamond nucleus and close to the interface. Results shown in Fig.7 indicate that the variation in  $\alpha$  nearly coincides with the contribution from the atoms at the interface, while the absorption from the nucleus approaches the absorption of crystalline diamond. The atoms at the interface determine the  $E_U$  for the whole composite. Defects at the interface (unpaired  $\text{sp}^2$  sites and dangling bonds) contribute negligibly to the optical transitions and the Urbach edge, as in pure  $a\text{-C}$  [38]. On the other hand,  $E_U$  for the diamond nanoinclusions takes quite high values ( $\sim 0.6$ ) and it is nearly constant as a function of  $\text{sp}^3$  fraction. This shows the significant structural disorder at the outer shell of the nanocrystals.

## 7. Summary

In this review, we have briefly presented some of our work on the energetics, stability, mechanical and optoelectronic properties of carbon-based nanostructured composites. These are materials consisting of a carbon crystalline nanoinclusion embedded in an amorphous carbon matrix. The inclusion ranges from a diamond crystallite to  $\text{sp}^3$  and  $\text{sp}^2$  crystalline conformations with negative and



positive curvature. The ability to control the mechanical and optoelectronic properties of these materials by varying the density of the embedding medium and the type and size of the crystalline inclusion opens up enormous possibilities for potential technological applications of carbon nanocomposites.

We found diamonds and schwarzites to be highly stable in dense amorphous carbon matrices, while the other  $sp^3$  and  $sp^2$  conformations are metastable. A considerable enhancement of the elastic moduli for  $nD/a-C$  and  $CNT/a-C$  was found as compared to pure  $a-C$  values with increasing density and inclusion size.  $a-C$  and  $nD/a-C$  of high density showed perfect elastic recovery, which was not the case for  $CNT/a-C$ . Beyond the elastic regime,  $nD/a-C$  fracture inter-grain and in a manner similar to pure  $a-C$ . Regarding the optoelectronic properties of  $nD/a-C$ , the matrix was shown to have a dominant role in forming both the EDOS and the dielectric function, with increasing  $sp^3$  fraction and density. Analysis of the optical response and the Urbach energy, showed that much of the disorder in the composites originates from the interface region.

### Acknowledgments

The authors wish to thank G. Kopidakis for useful discussions. This work was supported by the Ministry of National Education and Religious Affairs of Greece through the action "ΕΠΕΑΚ" (program "ΠΥΘΑΓΟΡΑΣ".) MF acknowledges support from the 'Gender Issue Incentive Funds' of the Cluster of Excellence in Munich, Germany.

### References

- [1] S. Subramoney, Adv. Mater. **10**, 1998 1157.
- [2] F. Banhart, Rep. Prog. Phys. **62**, 1999 1182.
- [3] J. Robertson, Mat. Sci. Eng. R **37**, 129 (2002).
- [4] M. O' Keeffe, G.B. Adams, and O.F. Sankey, Phys. Rev. Lett. **68**, 1992 2325.
- [5] D. Vanderbilt and J. Tersoff, Phys. Rev. Lett. **68**, 1992 511.
- [6] S. J. Townsend, T. J. Lenosky, D. A. Muller, C. S. Nichols, and V. Elser, Phys. Rev. Lett. **69**, 1992 921.
- [7] S. Iijima, Nature **354**, 1991 56.
- [8] G. A. J. Amaratunga, M. Chhowalla, C. J. Kiely, I. Alexandrou, R. Aharonov, R. M. Devenish, Nature **383**, 1996 321.
- [9] Y. Lifshitz, Th. Köhler, Th. Frauenheim, I. Guzmán, A. Hoffman, R. Q. Zhang, X. T. Zhou, and S. T. Lee, Science **297**, 2002 1531.
- [10] X. T. Zhou, Q. Li, F. Y. Meng, I. Bello, C. S. Lee, S. T. Lee, and Y. Lifshitz, Appl. Phys. Lett. **80**, 2002 3307.

- [11] Y. Yao, M. Y. Liao, Th. Köhler, Th. Frauenheim, R. Q. Zhang, Z. G. Wang, Y. Lifshitz, and S. T. Lee, Phys. Rev. B **72**, 2005 035402.
- [12] W. Kulisch, C. Popov , H. Rauscher , L. Sirghi , T. Sasaki , S. Bliznakov , F. Rossi, Diam. Relat. Mater. **17**, 2008 1116.
- [13] M.G. Fyta, I.N. Remediakis, and P.C. Kelires, Phys. Rev. B **67**, 2003 035423.
- [14] M.G. Fyta and P.C. Kelires, Appl. Phys. Lett. **86**, 2005 191916.
- [15] J. Tersoff, Phys. Rev. Lett. **61**, 1988 2879.
- [16] M. Mehl and D. Papaconstantopoulos, Phys. Rev. B **54**, 1996 4519.
- [17] R.E. Cohen, M. Mehl, and D. Papaconstantopoulos, Phys. Rev. B **50**, 1994 14694.
- [18] M.S. Tang, C.Z. Wang, C.T. Chan, and K.M. Ho, Phys. Rev. B **53**, 2996 979.
- [19] P.C. Kelires, Phys. Rev. Lett. **73**, 1994 2460.
- [20] C. Mathioudakis, P.C Kelires, Y. Panagiotatos, P. Patsalas, C. Charitidis, and S. Logothetidis, Phys. Rev. B, **65**, 2002 205203.
- [21] J.-Y. Raty, G. Galli, C. Bostedt, T. W. van Buuren, and L. J. Terminello, Phys. Rev. Lett. **90**, 2003 037401.
- [22] C. Mathioudakis, G. Kopidakis, P. C. Kelires, C. Z. Wang, K. M. Ho, Phys. Rev. B **70**, 2004 125202.
- [23] M.G. Fyta, I.N. Remediakis, P.C. Kelires, D.A. Papaconstantopoulos, Phys. Rev. Lett, **96**, 2006 185503.
- [24] P. Lu, X.P. Li, and R.M. Martin, Phys. Rev. Lett. **68**, 1992 1551;
- [25] P. Lu and W. Yang, Phys. Rev. B **49**, 1994 11421.
- [26] G. Vantarakis, C. Mathioudakis, G. Kopidakis, C. Z. Wang, K. M. Ho, and P. C. Kelires, Phys. Rev. B **80**, 2009 045307.
- [27] B. Winkler, C.J. Pickard, V. Milman, W.E. Klee, and G. Thimm, Chem. Phys. Lett. **312**, 1999 536.
- [28] F.D. Murnaghan, Proc. Natl. Acad. Sci. U.S.A. **30**, 1944 244.
- [29] F. Wooten, K. Winer, and D. Weaire, D. Phys. Rev. Lett. **54**, 1985 1392.
- [30] I.N. Remediakis, G. Kopidakis, and P.C. Kelires, Acta Mater. **56**, 2008 5340.

- [31] N.V. Galanis, I.N. Remediakis and G. Kopidakis. Phys. Status Solid **7**(5), 2010.
- [32] B. Paul, Transactions of the Metallurgical Society of AIME, 1960 36.
- [33] M. Fyta and P.C. Kelires, Diam. Relat. Mater. **16**, 2007 1676.
- [34] R.H. Telling, C.J. Pickard, M.C. Payne and J.E. Field, Phys. Rev. Lett. **84**, 2000 5160.
- [35] H. Chacham and L. Kleinman, Phys. Rev. Lett. **85**, 2000 4904.
- [36] C. Mathioudakis, G. Kopidakis, P.C. Kelires, P. Patsalas, M. Gioti, S. Logothetidis, Thin Solid Films **482**, 2005 151.
- [37] D. Franta, D. Nečas, L. Zajíčková, V. Buršíková, C. Cobet, Diamond Relat. Mat. **19**, 2010 114.
- [38] C. Mathioudakis, G. Kopidakis, P. Patsalas, and P. C. Kelires, Diam. Relat. Mater. **16**, 2007 1788.

## List of Table Captions

Table 1: Computational details of the composites with the various inclusions presented in this review.  $N_{tot}$ , are the total number of atoms.  $N_{cr}$ , and  $N_{am}$  are the number of atoms of the crystalline inclusion and the amorphous matrix, respectively.  $d$  and  $\lambda$  are the initial inclusion diameter and the filling ratio. Note, that not all inclusions are spherical; for these,  $d$  gives a rough estimate of their size. Next to the CNTs the chirality indices (n,m) are given.

Table 2: Elastic moduli (in GPa) for SWNT nanocomposites of different densities  $\rho$  (in  $\text{gcm}^{-3}$ ) and nanotube diameters  $d$  (in nm).

## List of Tables

Inclusion	$N_{tot}$	$N_{cr}$	$N_{am}$	d(nm)	$\lambda(\%)$
D	4096	464	3632	1.70	11
BC8	2744	325	2419	1.48	12
$6.8^2D$	3000	329	2671	1.79	11
PCCM	2592	304	2288	1.68	12
$C_{168}$	4536	636	3900	2.66	14
SWNT: (6,6)	460	144	316	0.82	31
SWNT: (7,10)	1486	292	1194	1.17	20
SWNT: (9,9)	1362	288	1074	1.24	21
SWNT: (12,12)	2097	480	1617	1.65	23
SWNT: (15,15)	2828	660	2168	2.06	23
SWNT: (20,20)	4910	1120	3790	2.75	23
MWNT(2 walls): (10,10)@(15,15)	3409	1177	2232	2.06	34
MWNT(3 walls): (5,5)@(10,10)@(15,15)	3645	1413	2232	2.06	37

Table 1

d(nm)	$\rho$	$C_{11}$	$C_{12}$	$C_{44}$	Y	B(GPa)
1.17	2.22	337	121	79	273	193
1.17	2.41	418	104	108	377	209
1.65	1.99	290	78	71	257	149
1.65	2.24	437	73	131	416	194
2.75	1.73	251	72	82	219	132
2.75	1.84	331	61	120	311	151

Table 2

## List of Figure Captions

Figure 1: Ball and stick models of carbon nanocomposites: (a) diamond, (b) schwarzite  $C_{168}$ , and (c) a (7,10) SWNT, embedded in  $a$ -C matrices of high (for diamond) and low (for  $C_{168}$  and the SWNT) densities. The atoms of the matrix and the embedded crystallite are indicated by white and black circles, respectively.

Figure 2: Formation energies for all carbon composites studied here. Panel (a) shows the  $na$ -C, apart from the SWNTs which are shown in (b) for various diameters denoted in the legend. Labels are self-explaining according to the text. Lines are fits to the points.

Figure 3: (a) Bulk ( $B$ ) and Young's ( $Y$ ) moduli, and (b) elastic constants for  $nD/a$ -C as functions of the total density ( $\rho$ ). The average diameter of the diamond inclusion is 1.7 nm.

Figure 4: (a) Bulk moduli for CNT/ $a$ -C of various diameters (shown in the legend) as functions of the density of the composite. The dotted line is a fit to the  $a$ -C data. (b) Comparison of  $B$  for SWNT and MWNT composites with diameters of 2.06 nm.

Figure 5: Left panel: Stress vs strain curves for structures under tensile load along the  $\{111\}$  direction (see text for details). Right panel: Ball and stick model for fracture in the  $nD/a$ -C for which the stress vs. strain curves are shown on the left. Atoms are shaded according to the legend. Large spheres (with label (b)) denote atoms with broken bonds. The snapshot corresponds to the maximum stress, at which bonds have started to break.

Figure 6: EDOS (left) and calculated  $\varepsilon_2$  (right) of  $nD/a$ -C with  $sp^3$  fractions and densities (a) 88 % and  $3.24 \text{ g cm}^{-3}$ , (b) 71% and  $2.91 \text{ g cm}^{-3}$ , and (c) 51% and  $2.58 \text{ g cm}^{-3}$ , respectively. The black, blue, and red lines refer to the total function, and the inclusion and  $a$ -C matrix projected contributions, respectively. The Fermi level is at 0 eV.

Figure 7: (a) Variation of  $E_U$  in  $nD/a$ -C as a function of the  $sp^3$  fraction in the matrix (AM). Filled circles and squares are the contributions from the inclusion and the matrix, respectively. Open circles are values from core atoms in the inclusion. Diamond and triangle are values for diamond and *amorphous diamond*, respectively. Light gray line shows  $E_U$  in pure  $a$ -C. (b) Breakdown of  $\alpha$  (dashed-dotted red line) of a  $nD/a$ -C with 88%  $sp^3$  fraction and  $3.24 \text{ g cm}^{-3}$  in the  $a$ -C matrix into contributions from the core (black solid line) and the interface (black dashed line) atoms. Solid brown line indicates the calculated absorption of diamond.

## List of Figures

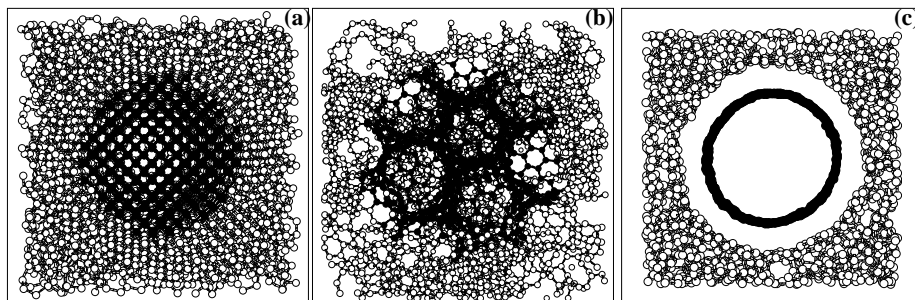


Figure 1

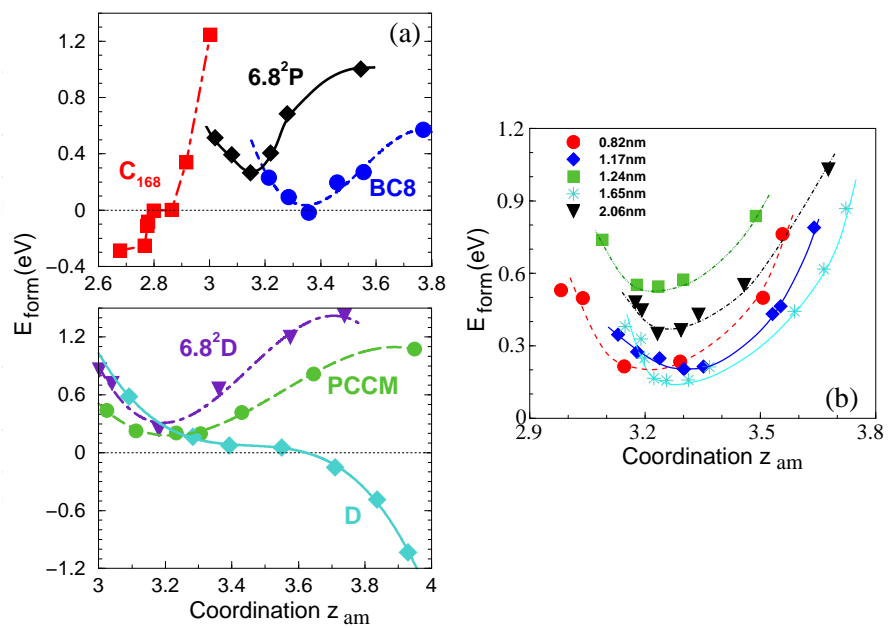


Figure 2

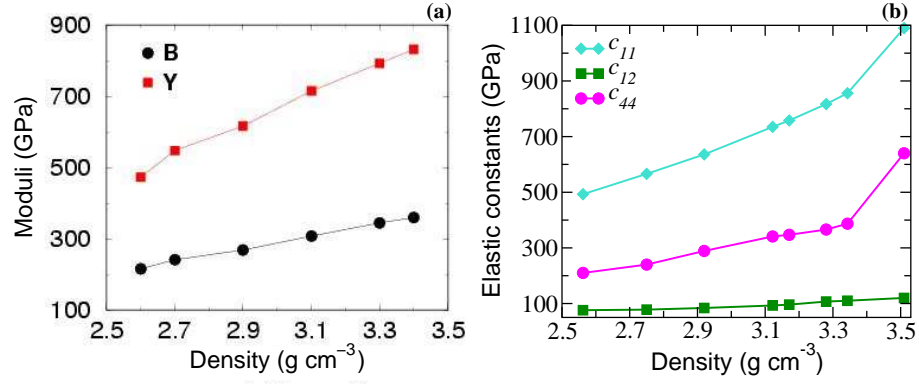


Figure 3

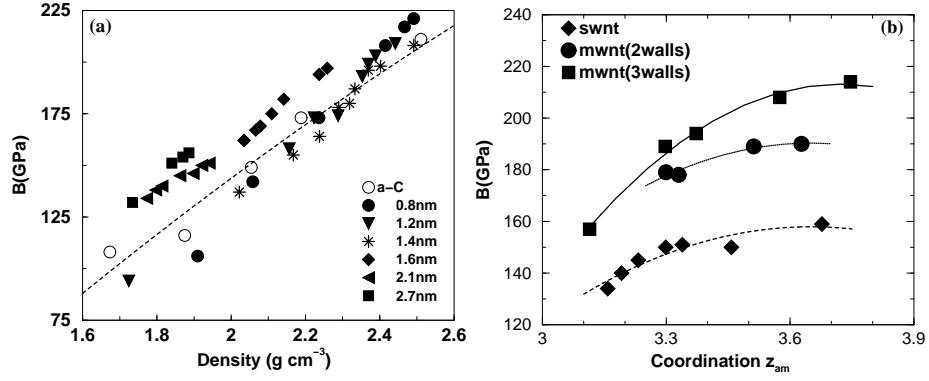


Figure 4

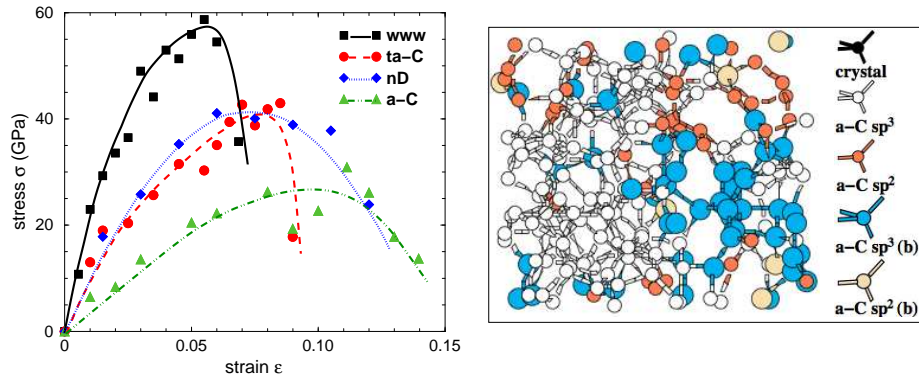


Figure 5



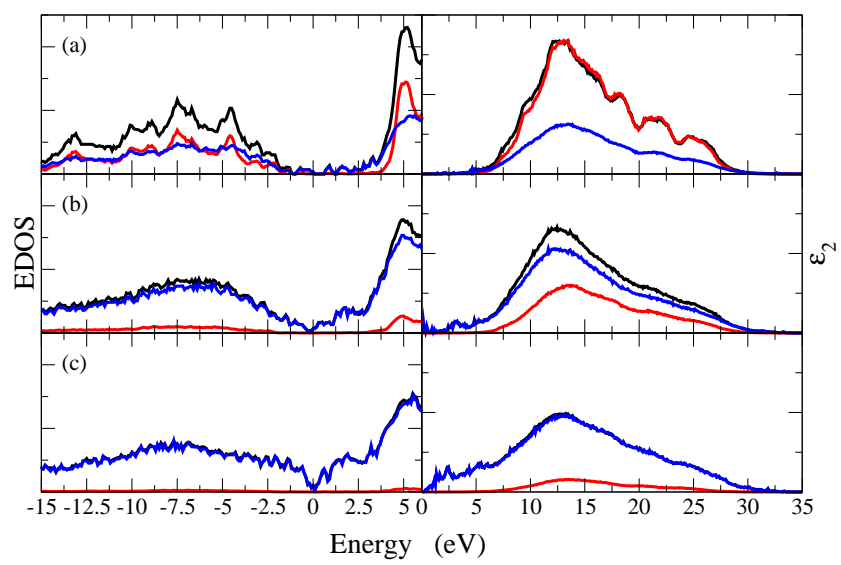


Figure 6

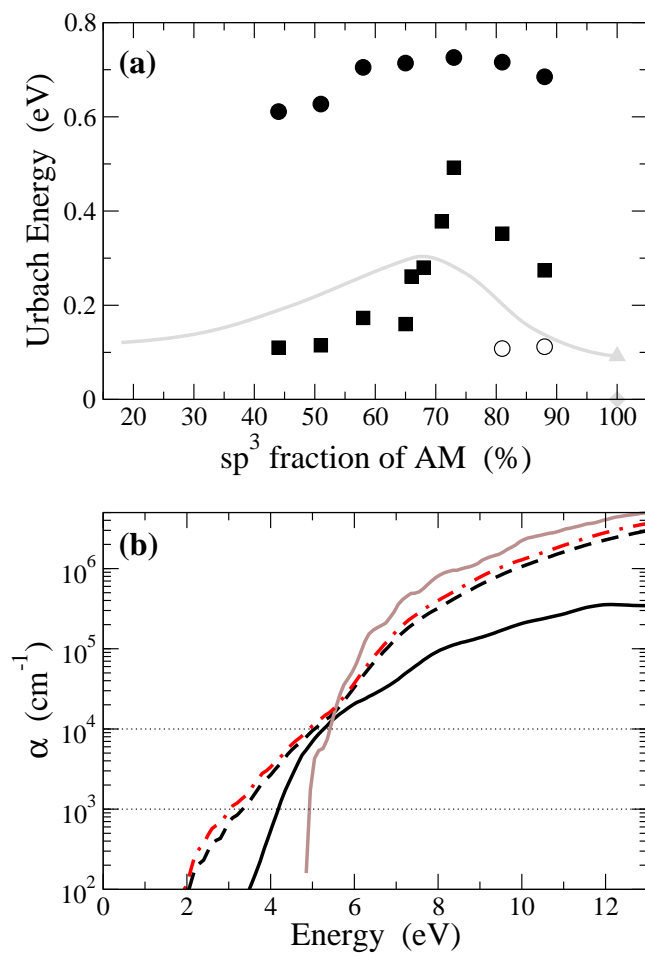


Figure 7